

AUS Repository

Effect of Gd, V, and Y Alloying on the Corrosion Properties of Fe-Mn-Ni-Al Fe-based Shape Memory Alloy

Item Type	Article;Peer-Reviewed;Published version
Authors	Mustafa, Faisal;Ahmad, Shahbaz;Hassan, Arhum;Egilmez, Mehmet;El Khatib, Sami;Ibrahim, Taleb
Citation	Mustafa, F., Ahmad, S., Hassan, A., Egilmez, M., El-Khatib, S., & Ibrahim, T. (2024). Effect of Gd, V, and Y Alloying on the Corrosion Properties of Fe-Mn-Ni-Al Fe-based Shape Memory Alloy. Journal of Physics: Conference Series, 2751(1), 012011. https://doi.org/10.1088/1742-6596/2751/1/012011
DOI	10.1088/1742-6596/2751/1/012011
Publisher	IOP Science
Rights	Attribution 3.0 International
Download date	2026-05-20 17:27:13
Item License	http://creativecommons.org/licenses/by/3.0/
Link to Item	https://hdl.handle.net/11073/33306

PAPER • OPEN ACCESS

Effect of Gd, V, and Y Alloying on the Corrosion Properties of Fe-Mn-Ni-Al Fe-based Shape Memory Alloy

To cite this article: Faisal Mustafa *et al* 2024 *J. Phys.: Conf. Ser.* **2751** 012011

View the [article online](#) for updates and enhancements.

You may also like

- [Loading influence on the corrosion assessment during stress-induced martensite reorientation in nickel-titanium SMA](#)
Mahdi Mohajeri, Raymundo Case, Behrouz Haghgouyan *et al.*
- [Corrosion resistance of nonnickel shape memory alloy](#)
E O Nasakina, M A Sudarchikova, A M Tsareva *et al.*
- [The Effect of the addition of Ta, Zr and in on the corrosion behaviour of CuAlMn alloys prepared via powder metallurgy](#)
Duaa Amer Ali, Ali Hubi Haleem and Haydar H.J. Jamal Al-Deen

Effect of Gd, V, and Y Alloying on the Corrosion Properties of Fe-Mn-Ni-Al Fe-based Shape Memory Alloy

Faisal Mustafa^{1,2*}, Shahbaz Ahmad^{1,2}, Arhum Hassan^{1,2}, Mehmet Egilmez^{1,2*}, Sami El-Khatib^{1,2}, Taleb Ibrahim^{2,3}

¹ Department of Physics, American University of Sharjah, Sharjah 26666, United Arab Emirates

² Materials Science and Engineering Program, American University of Sharjah, Sharjah 26666, United Arab Emirates

³ Department of Chemical Engineering, American University of Sharjah, Sharjah 26666, United Arab Emirates

*Corresponding authors' e-mail: b00090953@aus.edu, megilmez@aus.edu

Abstract. Shape Memory Alloys (SMA) are widely utilized in numerous industrial applications nowadays. Significant attention has been given to Fe-based SMA in civil engineering applications due to their high strength and reasonable cost. Researchers are striving to improve the corrosion resistance of these alloys so they can be utilized in marine environments. This article focuses on the effect of Gd, V, and Y alloying on FeMnNiAl based SMA. The phases and morphological effects were characterized using X-Ray diffractometer (XRD), Scanning Electron Microscopy (SEM), and Energy Dispersive Spectroscopy (EDS). To examine the corrosive nature of the Fe-based SMA system, a potentiodynamic analysis and electrochemical impedance spectroscopy (EIS) tests were performed in 3.5% NaCl solution. Results show that the addition of Gd rare earth metal has improved the overall corrosion efficiency of Fe-based SMAs by 48%.

1. Introduction

Multi-principle element alloying techniques have been utilized during the last two decades due to their advantage in producing mechanical, electrical, and magnetic functionalities [1–4]. One of the mechanical functionalities of great interest is the shape memory effect (SME) and superelasticity (SE). Shape memory materials (SMMs) are a class of materials that possess the ability to regain their initial shape after undergoing a considerable and seemingly plastic deformation whenever a specific stimulus is applied. In SMMs, properties such as superelasticity (in alloys) and visco-elasticity (in polymers) can be observed under certain conditions. Shape memory alloys (SMAs) go through a reversible martensitic phase transition from the high-symmetry austenite to low-symmetry martensite phase under the influence of temperature or stress field, resulting in the SME and superelasticity, respectively. Since the discovery of the shape memory effect in the 1970s by Wayman [5], The functional and mechanical properties (such as pre-stressing, damping capacity, and exceptional workability) of Fe-based shape memory alloys (SMAs) have demonstrated their potential as a viable option for various industrial applications [6][7][8]. In particular, SMAs are often explored for use in civil engineering applications since they are a more cost-effective option than their non-ferrous counterparts.

Fe-Mn-Ni-Al is a new and promising SMA candidate which was first reported by Omori et al. in 2011 [9]. Numerous researchers worldwide have conducted extensive studies on Fe-Mn-based shape memory alloys (SMAs) with the aim of enhancing their mechanical and corrosion characteristics



[10][11][12][13][14][15][16][17][18]. This group of materials exhibits excellent superelastic characteristics over a broad temperature spectrum. This Fe-based Shape Memory Alloy (SMA) experiences a thermoelastic transformation across a broad temperature spectrum, involving a transition from the Body Centered Cubic (BCC) austenitic phase to a Face Centered Cubic (FCC) martensitic phase. This transformation is primarily attributed to the formation of nano-sized precipitates within the matrix [19][20][21][22]. Moreover, studies showed a good corrosion resistance in this alloy which is on par with that of stainless steels owing to the addition of Nickel and Chromium elements [23]. This makes Fe-based SMA with Cr and Ni addition a better candidate in coastal/offshore engineering construction applications which have chloride environments [24]. In particular, Lin et al. showed enhancement of corrosion resistance in Fe-Mn-based SMA when Cr and Ni are introduced to the structure [25]. Moreover, Jaehoon et al. reported that the corrosion resistance of the SMA was improved with the addition of Mn and Cr in Fe-based SMA due to the formation of a stable passivation oxide layer in alkaline environments for different pH [26]. The enhancement of corrosion resistance by alloying is reported not only for Fe-based SMA but also by other SMA alloys. For example, Cu-Al-Ni-based SMA showed a reduction in corrosion rate due to the presence of 1.5 wt.% of Ti [27].

Recently, the addition of rare earth elements has shown an improvement in the corrosion resistance of SMA alloys. Xin et al. studied the influence of Nd on the corrosion behavior of Cu-Al-Ni high-temperature SMA [28]. The authors reported a reduction in the corrosion current density of the SMA alloy owing to the presence of acicular martensite with the addition of Nd. Nawal and Abdul studied the alloying effect of titanium on the corrosion resistance of Cu-based SMA [29]. The presence of Ti in the passivation layer enhanced the alloy resistance from the aggressive action of Cl⁻ ions in the NaCl solution compared to the alloy without Ti Addition.

The current work focuses on the influence of adding various metals including rare earth metals (Gd, V, and Y) on the corrosion behavior of Fe-Mn-Ni-Al-based SMA.

2. Materials and Methods

All Fe-based SMA materials were induction melted as per the composition given in Table 1. After solidification, the samples were homogenized at 1200 °C for 24 hours in an inert Ar atmosphere. These homogenized samples were machined using wire Electric Discharge Machining (EDM) according to the desired dimension of 1cm x 1cm and having a thickness of 1mm. The samples were ground and polished for corrosion and microstructural study.

Table 1. Alloying composition for the Fe-based SMA (at. %).

Sample ID	Fe	Mn	Ni	Al	Add-on
Fe-SMA	43.5	34	7.5	15	-
Fe-Gd-SMA	40.7	32.4	7.3	6.8	12.9
Fe-V-SMA	42.4	33.6	9.7	8.5	5.7
Fe-Y-SMA	41.1	33.7	8.2	7.5	9.5

Phase and crystallographic analyses of all samples were performed using X-Ray Diffractometer (Malvern Panalytical's X'Pert³, Malvern, UK). Morphological and elemental composition were investigated with Scanning Electron Microscope (TESCAN VEGA 3) coupled with Energy-Dispersive X-ray Spectroscopy (Tescan, Brno, Czechia). Drop Shape Analyzer (DSA-100, KRUSS, Matthews, NC, USA) was utilized to carry out the water contact angle measurements.

The accelerated potentiodynamic corrosion tests and Electrochemical Impedance Spectroscopy (EIS) were performed in three electrode setup connected to CHI-660E Potentiostat (CH Instruments, USA). The corresponding three electrode setup was composed of Platinum coil (counter electrode), Ag/AgCl filled with 3M KCl solution (reference electrode) and the studied samples with a 1cm² exposed area as a working electrode. All three electrodes were immersed in 3.5 wt.% NaCl electrolyte.

3. Results and Discussions

3.1. X-Ray Diffractometry

XRD patterns of all the FeMnNiAl family of alloys under observation showed a dual phase structure consisting of a BCC and FCC phase, as shown in Fig. 1. Prominent FCC (γ) peaks appeared at 2θ values of 43° and 49° whereas for BCC (α) peaks were observed at 45° and 65° [30][31]. BCC was a dominant phase in the structure regardless of alloy addition. It is because, inherently, FeMnNiAl is in a dual phase, i.e., a secondary phase inside the matrix phase. So, the addition of further alloys results in preferential alloying with one phase, which was confirmed via EDS area mapping. This affinity towards a preferred state can be illustrated with the help of a 5-element phase diagram which is beyond the scope of the current work. But this dual-phase structure has its impact on the corrosion properties of the materials. Usually, it is easy to predict the corrosion behavior of an alloy with a single phase under certain circumstances. However, with a double phase, one should consider not only the intrinsic behavior of each phase but also understand the effect of one phase on another. The dual phases can have different chemical and electronegative potentials, which can result in a galvanic cell formation and might also result in severe corrosion of one phase than the other. The morphology and distribution (phase and elemental) of these phases are further elaborated using SEM and EDS.

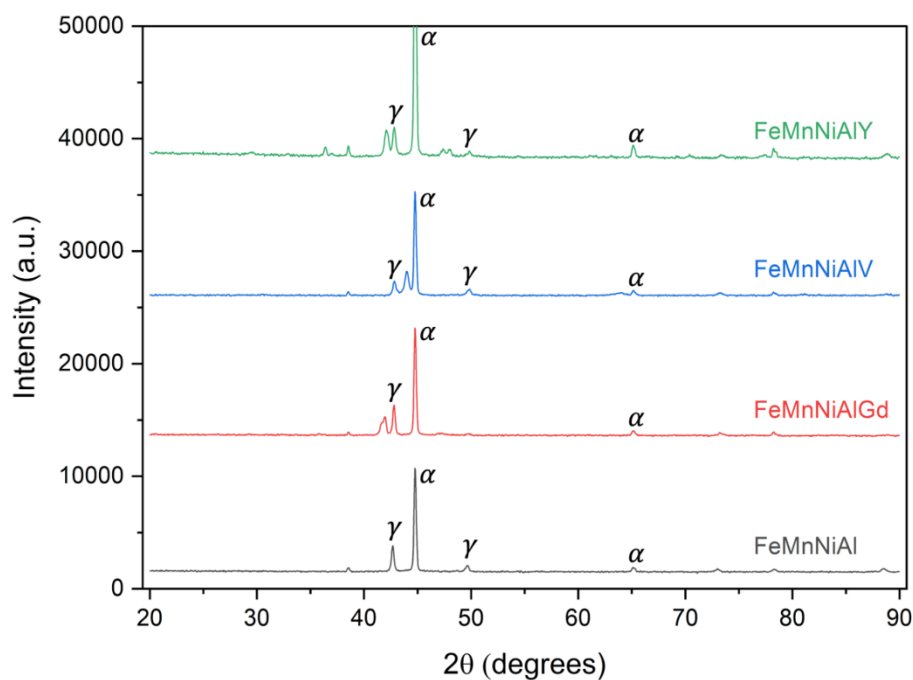


Figure 1. XRD patterns of the FeMnNiAl SMA with the addition of different alloying elements.

3.2. Scanning Electron Microscopy

Scanning Electron Microscopy (SEM) images showed the dual phase structures having a matrix (α) and a secondary phase (γ) (Fig. 2). Figure 2(a) shows the dual phase structure of the FeMnNiAl system where the secondary phase has a dendritic (lamellar) structure. The phases have distinct chemical compositions due to which two unique electronegativity potentials exist and will result in corrosion on the phase boundary between the two phases, shown in Figure 2(e). In the Fe-Gd system, the phases are still dual but have slightly bigger secondary phase grains inside the structure, as seen in Figure 2(b).

Whereas, after corrosion (Fig. 2(f)) the matrix phase seems more oxidized (corroded) than the secondary phase and it is further validated by EDS results.

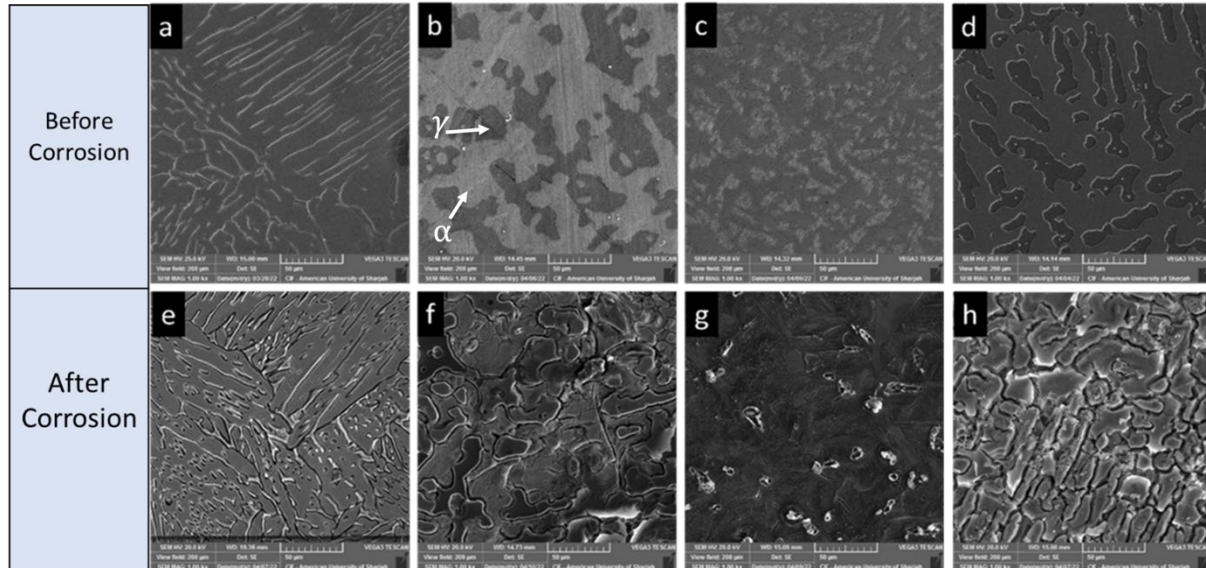


Figure 2. SEM images of (a, e) base alloy (FeMnNiAl), alloyed with (b, f) Gd, (c, g) V, and (d, h) Y. SEM for images (a-d) were collected before corrosion tests and (e-h) after corrosion tests.

The SEM image of the Fe-V sample before corrosion is shown in Figure 2(c); this sample has a dual-phase structure with a fine distribution of the secondary phase in the matrix. The contrast variation shows a slight change in phase distribution and hence instead of galvanic corrosion, pitting is observed after the corrosion attack. The SEM of the Fe-V sample after corrosion is shown in Figure 2(g) having pits that are clearly visible on the surface. Fe-Y sample with large grains of secondary phase (Fig. 2(d)) showed severe uniform corrosion under seawater environment (Fig. 2(h)). It is hard to identify the phases after corrosion. Therefore, EDS was performed to show the phase distribution with an elemental variation using elemental area mapping.

By analyzing all the SEM images, it was observed that the Fe-Gd sample was the least corroded sample as indicated by the surface oxides after corrosion. The base sample Fe-SMA showed better corrosion resistance than Fe-V and Fe-Y alloys as the corrosion product is mostly on the phase boundaries. Fe-V has the worst corrosion resistance as revealed by the formation of pits in the structure, which are dangerous from an application point of view. Fe-Y is also not very corrosion resistant but has a relatively better corrosion resistance than Fe-V.

3.3. Energy Dispersive X-ray Spectroscopy

Energy Dispersive X-ray Spectroscopy (EDS) analysis was performed to show the elemental composition of the overall alloy (EDS area mapping) and the elemental composition of each phase (point EDS). The overall elemental composition through area mapping of each alloy is given in Table 1, while the elemental phase compositions through point scan on each phase for each alloy before and after corrosion is given in Table 2 and Table 3, respectively.

Table 2. Phase compositions were obtained using point scans for the different phases in each alloy system before corrosion (wt. %).

Sample ID	α Fe	γ Fe	α Mn	γ Mn	α Ni	γ Ni	α Al	γ Al	α Add.	γ Add.
-----------	-------------	-------------	-------------	-------------	-------------	-------------	-------------	-------------	---------------	---------------

Fe-SMA	46.4	36.2	37.4	27.1	7.7	19.5	8.5	17.2	-	-
Fe-Gd-SMA	32.8	50.0	26.5	40.0	9.7	4.7	8.0	5.3	23.0	-
Fe-V-SMA	40.3	41.8	30.9	36.1	11.6	9.9	10.9	7.7	6.3	4.5
Fe-Y-SMA	36.9	49.9	30.8	39.3	10.0	4.9	8.2	5.9	14.0	-

Table 3. Phase compositions were obtained using point scan for the different phases in each alloy system after corrosion (wt. %).

Sample ID	α Fe	γ Fe	α Mn	γ Mn	α Ni	γ Ni	α Al	γ Al	α Add.	γ Add.	α O	γ O
Fe-SMA	44.9	33.5	36.6	23.8	7.5	22.6	7.7	20	-	-	3.2	-
Fe-Gd-SMA	13.1	41.8	4.9	32.5	53.9	10.9	2.2	4.3	3.8	-	21.4	10.4
Fe-V-SMA	31.9	41.2	21.8	37.4	12.9	6.6	8.9	4.3	7.6	4.3	16.2	5.7
Fe-Y-SMA	10.8	39.2	4.6	27.5	56.8	16.6	2.5	3.8	0.7	-	24.6	12.9

Fe-SMA (FeMnNiAl) showed a dual-phase structure where both phases have distinct elemental compositions. The matrix phase (α) is enriched in Fe and Mn while the secondary phase (γ) has Ni and Al in abundance. Point EDS analysis of each phase shows the individual elemental composition of each phase in the Fe-SMA (Table 2). These phase compositions result in corrosion at the phase boundaries due to differences in chemical potential and the formation of a galvanic cell. The EDS mapping of each phase after corrosion (Table 3) showed that the matrix phase is corroding as a sacrificial anode where the oxide formation of Fe, Mn, Ni, and Al can be observed easily, and the oxygen content is only observed in the matrix phase.

The Fe-Gd sample also has compositional variation across both phases. In this alloy, unlike Fe-SMA, Fe and Mn form the secondary phase while Ni, Al, and Gd have higher concentrations in the matrix phase. The exact phase compositions are shown in Table 2, where Gd is forming the matrix phase along with Ni and Al and is not present in the secondary phase. At the same time, all other elements are present in the secondary phase with higher weight percentages of Fe and Mn. Table 3 represents the elemental variation along with oxide content in each phase after corrosion, showing that the matrix phase has more oxide content and hence it was deduced that more corrosion occurred in this phase. A similar observation was made from the SEM images (Fig. 2). Oxides of Fe and Mn are the main corrosion products in the matrix phase and at the same time, the oxides of secondary phase are also of similar elements but with lesser concentration.

Unlike Fe-Gd-SMA, Fe-V shows composition-based phase duality, but V is present in both phases. The concentration of V is more in the matrix phase along with Ni and Al than in the secondary phase. The elemental variation along the two phases is very close yet different from each other. All the elements are present in both the phases with a slight variation of Fe and Mn abundance in the secondary phase and vice versa. Due to this, the chemical potential difference between the phases is not prominent and such kinds of phases will result in either uniform or pitting corrosion. The EDS analysis of both phases before and after corrosion depicts that the oxides of Fe and Mn are abundant in the secondary phase, while oxides of Al and Ni are formed in the matrix phase. But overall, more oxide products appeared in the matrix region.

The EDS result of Fe-Y alloy having a secondary phase containing Fe and Mn in abundance is shown in Table 2. Ni and Al are in a higher concentration in the matrix phase (α) along with Y. The presence of yttrium in this dual-phase system of FeMnNiAl SMA is similar to that of Gd as it is only present in the matrix phase along with major concentrations of Ni and Al. The individual phase composition verifies the presence of Y in the matrix phase but not in the γ -phase. Table 3 shows the EDS analysis of the Fe-Y sample after corrosion showing oxidation on the surface, majorly in the matrix region. Fe, Mn, and Ni were heavily oxidized along with Y in the matrix phase while Ni remains stable while lesser oxide formation is found on the γ -phase, having no Y, concluding that Y is accelerating the oxide

formation. Hence severe oxidation is observed in this alloy after corrosion in the seawater; both phases form oxides that are not passive, and the corrosion properties of this system are not as good as the other studied compositions.

The water contact angle (WCA) method was utilized to conduct a surface wettability analysis on all samples. The hydrophobic nature of Fe-SMA, Fe-Gd-SMA, Fe-V-SMA, and Fe-Y-SMA polished electrode surfaces is demonstrated in Figure 3, where the water droplet in contact with each material exhibits a contact angle of 110.2°, 110°, 110.5°, and 113.2°, respectively. The hydrophobic surface impedes the adhesion of aqueous corrosive agents, thereby endowing the surface with favorable anticorrosive characteristics [32].

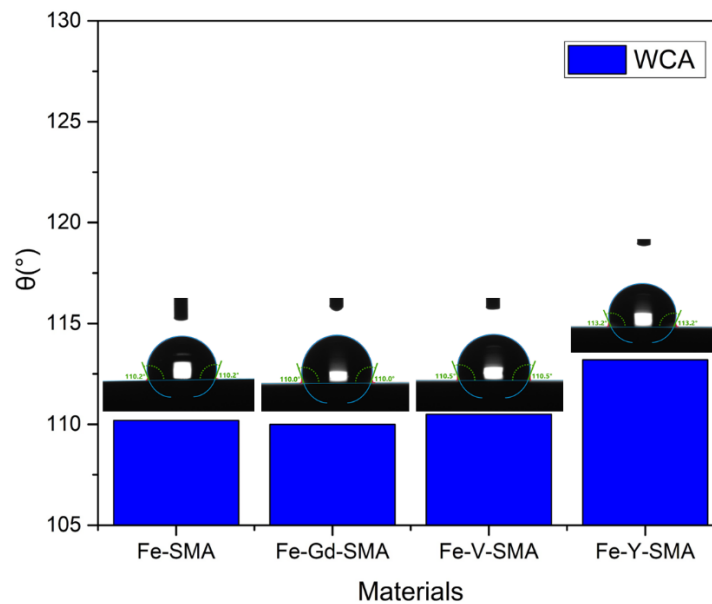


Figure 3. Water contact angle measurements of SMA samples

3.4. Corrosion Analysis

The anti-corrosive properties of Fe-based SMAs were investigated to further verify the argument based on microstructural analysis. Figure 4 (a-d) illustrates the Potentiodynamic polarization curves for all SMA samples. The relationship between corrosion potential (V_{corr}) and corrosion current (I_{corr}) were determined by fitting a slope through Tafel region in polarization curve where E vs $\log j$ is linear over a significant range. From Ohm's law $I_{corr} = E/R_p$, where "E" is the difference between cathode and anode potential, " R_p ", is the polarization resistance during potentiodynamic measurement, and is an arithmetic sum of the solution resistance of the corrosive medium (R_s) and the interfacial charge transfer resistance (R_{ct}) of the immersed working metal electrode. Table 4 shows that R_{ct} , measured from the EIS Nyquist plots in (Figure 5(a)) by fitting an equivalent Randle's circuit (Figure 5(b)) exhibits a higher value for Fe-Gd-SMA (7458 $\Omega \cdot \text{cm}^2$) followed by Fe-SMA (6964 $\Omega \cdot \text{cm}^2$) sample while Fe-Y-SMA (1267 $\Omega \cdot \text{cm}^2$) and Fe-V-SMA (1047 $\Omega \cdot \text{cm}^2$) showed comparatively small resistance values.

The corrosion rate (CR) and protection efficiency (P.E) of all SMA samples were determined from Figure 4 (a-d) using the following equations [33][34,35].

$$CR = \frac{j_{corr} M}{DZF} \quad (1)$$

Where j_{corr} (mA/cm^2) is the corrosion current density, M (g/mol) is the equivalent molecular weights of elements in the alloy, D is the density of corroding metal (g/cm^3), Z is the metal valency, and F is the Faraday constant (96485 As/mol).

$$P.E\% = \frac{j_{corr} - j'_{corr}}{j_{corr}} \quad (2)$$

Herein, j_{corr} and j'_{corr} denote the corrosion current densities prior to and subsequent to the incorporation of alloying elements (Gd, V, and Y), respectively.

The anticorrosive property of material is evaluated by its protection efficiency (P.E), which is determined by the relative decrease in the current density (j) of the sample in comparison to the Fe-SMA reference. The Fe-Gd-SMA specimen displays superior anti-corrosive properties relative to other specimens, as inferred from equations 1 and 2, with corresponding CR and P.E values of 8.9 $\mu\text{m}/\text{year}$ and 48 % relative to reference Fe-SMA substrate. However, a substantial increase in CR of 14.9 and 14.8 $\mu\text{m}/\text{year}$ was observed for Fe-V-SMA and Fe-Y-SMA showing poor corrosion properties with higher corrosion rates.

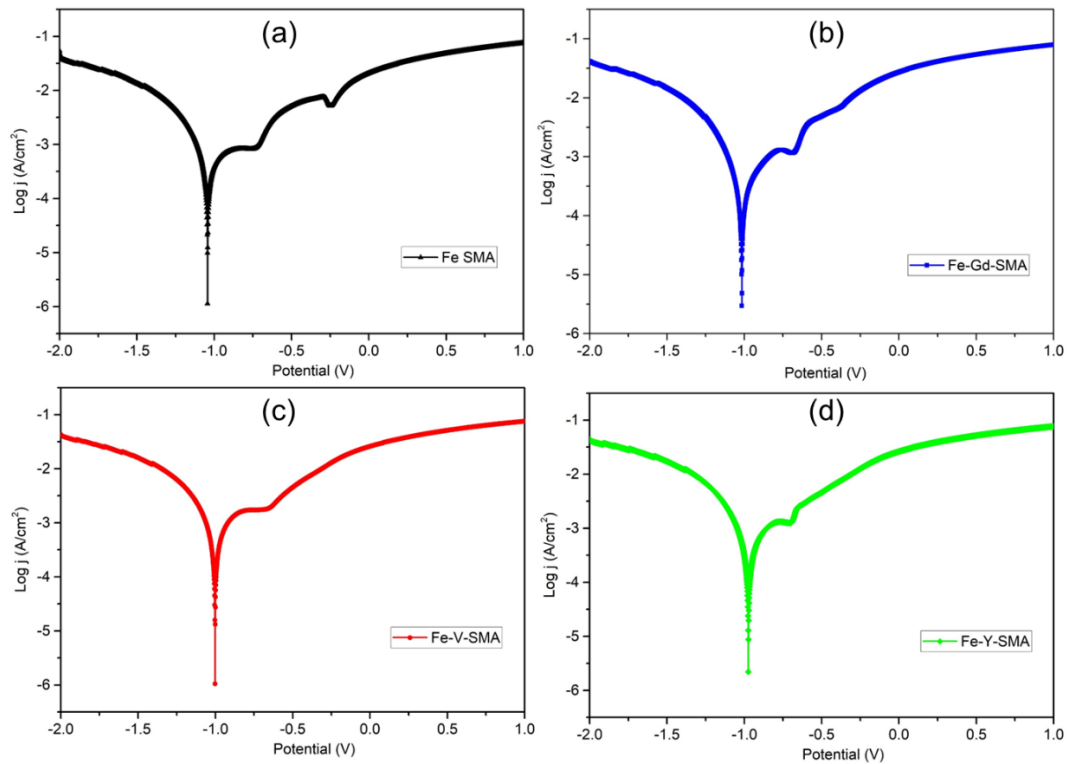


Figure 4. Electrochemical potentiodynamic polarization plots: (a) Fe-SMA, (b) Fe-Gd-SMA, (c) Fe-V-SMA, (d) Fe-Y-SMA.

Table 4. Summary of electrochemical corrosion parameters extracted from Tafel and EIS plots.

Samples	E_{corr} (V)	j_{corr} ($\mu\text{A}/\text{cm}^2$)	CR $\mu\text{m}/\text{Year}$	R_{ct} ($\Omega.\text{cm}^2$)	P.E (%)
Fe-SMA	-1.042	540	12.1	6964	Reference
Fe-Gd-SMA	-1.016	283	8.9	7458	+48
Fe-V-SMA	-1.004	639	14.9	1047	-18
Fe-Y-SMA	-0.968	598	14.8	1267	-11

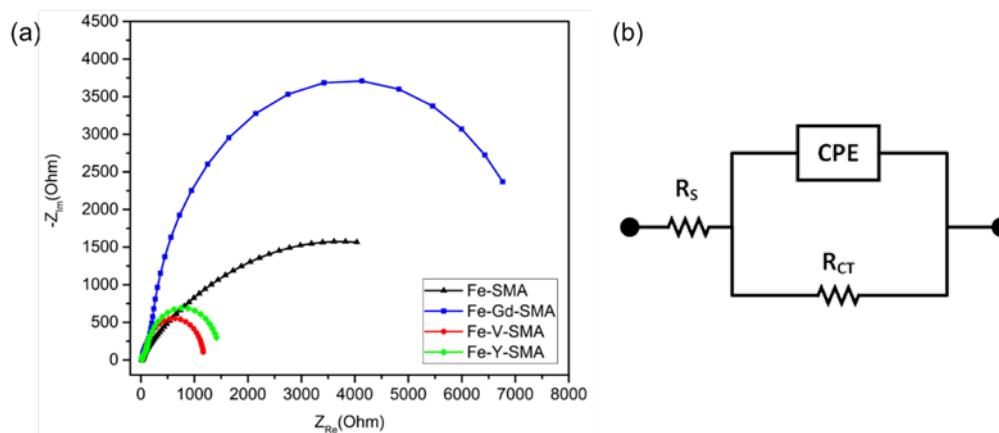


Figure 5. (a). EIS Nyquist plots of Fe-based SMAs, (b) Equivalent Randle's circuit.

4. Conclusions

In this work, alloying of transition metals and rare earth elements (Gadolinium, Vanadium and Yttrium) in FeMnNiAl shape memory alloy was carried out through induction melting. The structural and compositional characteristics of the alloys were studied by XRD and SEM. Electrochemical investigations were performed using Tafel polarization and Electrochemical Impedance Spectroscopy in 3.5 wt% NaCl solution to replicate the seawater environment. The SEM images indicated the formation of two phases in each of these alloys, verified using XRD. XRD analysis shows that these phases correspond to two different crystal structures, i.e., BCC and FCC. Tafel polarization plots indicated that the addition of Gd in FeMnNiAl SMA enhanced the anticorrosion properties, such as the slowest corrosion rate of 8.9 $\mu\text{m}/\text{Year}$, which was much better as compared to its other reference alloys. The presence of Gd helped in forming a self-passivating oxide layer during accelerated corrosion. The SEM/EDS analysis also showed low corrosion products. On the other hand, the addition of V and Y creates a potential difference between the phases. This results in a high charge transfer rate which makes the alloy less suitable for corrosion applications. The protection efficiency of the alloy made by the addition of Gd is approximately 50%, while the addition of V and Y resulted in negative efficiencies. The study concludes that the addition of Gd in the FeMnNiAl system has shown promising results for anticorrosive applications in the marine environment.

References

- [1] Egilmez M and Abuzaid W 2021 Magnetic , electrical and mechanical properties of - entropy alloy *Sci. Rep.* 1–12
- [2] Abuzaid W, Egilmez M and Chumlyakov Y I 2021 TWIP – TRIP effect in single crystalline VFeCoCrNi multi-principle element alloy *Scr. Mater.* **194** 113637
- [3] Mustafa F, Egilmez M, Abuzaid W, El-khatib S, Nawaz T and Ahmad S 2023 Strange Metallicity and Magnetic Order in the CoNi (Cr / V) Medium-Entropy Alloy System 1–14
- [4] George E P, Raabe D and Ritchie R O 2019 High-entropy alloys *Nat. Rev. Mater.* **4** 515–34
- [5] Wayman C M 1971 On memory effects related to martensitic transformations and observations in β -brass and Fe3Pt *Scr. Metall.* **5** 489–92
- [6] Sato A, Chishima E, Soma K and Mori T 1982 Shape memory effect in $\gamma \rightleftharpoons \epsilon$ transformation in Fe-30Mn-1Si alloy single crystals *Acta Metall.* **30** 1177–83
- [7] Sato A, Chishima E, Yamaji Y and Mori T 1984 Orientation and composition dependencies of shape memory effect in Fe-Mn-Si alloys *Acta Metall.* **32** 539–47
- [8] Janke L, Czaderski C, Motavalli M and Ruth J 2005 Applications of shape memory alloys in

- civil engineering structures—Overview, limits and new ideas *Mater. Struct.* **38** 578–92
- [9] Fernández-Domene R M, Blasco-Tamarit E, García-García D M and García-Antón J 2013 Passive and transpassive behaviour of Alloy 31 in a heavy brine LiBr solution *Electrochim. Acta* **95** 1–11
- [10] HU B, BAI P, DONG Z and CHENG J 2009 Effect of Cu addition on corrosion resistance and shape memory effect of Fe-14Mn-5Si-9Cr-5Ni alloy *Trans. Nonferrous Met. Soc. China* **19** 149–53
- [11] Söderberg O, Liu X W, Yakovenko P G, Ullakko K and Lindroos V K 1999 Corrosion behaviour of Fe–Mn–Si based shape memory steels trained by cold rolling *Mater. Sci. Eng. A* **273** 543–8
- [12] Ariapour A, Yakubtsov I and Perovic D D 1999 Effect of nitrogen on shape memory effect of a Fe–Mn-based alloy *Mater. Sci. Eng. A* **262** 39–49
- [13] Wan J, Huang X, Chen S and TY H X Z 2002 Effect of nitrogen addition on shape memory characteristics of Fe–Mn–Si–Cr alloy *Mater. Trans.* **43** 920–5
- [14] Charfi A, Bouraoui T, Feki M, Bradai C and Normand B 2009 Surface treatment and corrosion behaviour of Fe–32Mn–6Si shape memory alloy *Comptes Rendus Chim.* **12** 270–5
- [15] Patriarca L, Abuzaid W, Carlucci G, Belevi F and Casati R 2021 Pseudoelasticity in FeMnNiAl shape memory alloy lattice structures produced by Laser Powder Bed Fusion *Mater. Lett.* **302** 130349
- [16] Sidharth R, Mohammed A S K, Abuzaid W and Sehitoglu H 2021 Unraveling frequency effects in shape memory alloys: NiTi and FeMnAlNi *Shape Mem. Superelasticity* **7** 235–49
- [17] Abuzaid W, Wu Y, Sidharth R, Brenne F, Alkan S, Vollmer M, Krooß P, Niendorf T and Sehitoglu H 2019 FeMnNiAl Iron-Based Shape Memory Alloy: Promises and Challenges *Shape Mem. Superelasticity* **5** 263–77
- [18] Abuzaid W and Sehitoglu H 2019 Shape memory effect in FeMnNiAl iron-based shape memory alloy *Scr. Mater.* **169** 57–60
- [19] Vollmer M, Kriegel M J, Walnsch A, Klemm V, Leineweber A and Niendorf T 2019 On the microstructural and functional stability of Fe-Mn-Al-Ni at ambient and elevated temperatures *Scr. Mater.* **162** 442–6
- [20] La Roca P, Baruj A, Sobrero C E, Malarria J A and Sade M 2017 Nanoprecipitation effects on phase stability of Fe-Mn-Al-Ni alloys *J. Alloys Compd.* **708** 422–7
- [21] Tseng L W, Ma J, Hornbuckle B C, Karaman I, Thompson G B, Luo Z P and Chumlyakov Y I 2015 The effect of precipitates on the superelastic response of [1 0 0] oriented FeMnAlNi single crystals under compression *Acta Mater.* **97** 234–44
- [22] Omori T, Nagasako M, Okano M, Endo K and Kainuma R 2012 Microstructure and martensitic transformation in the Fe-Mn-Al-Ni shape memory alloy with B2-type coherent fine particles *Appl. Phys. Lett.* **101** 231907
- [23] Cladera A, Weber B, Leinenbach C, Czaderski C, Shahverdi M and Motavalli M 2014 Iron-based shape memory alloys for civil engineering structures: An overview *Constr. Build. Mater.* **63** 281–93
- [24] Wang X X and Zhao L C 1992 The effect of thermal-mechanical training on the formation of stress-induced ϵ martensite in an Fe□Mn□Si□Ni□Co alloy *Scr. Metall. Mater.* **26** 1451–6
- [25] Lin H C, Lin K M, Lin C S and Ouyang T M 2002 The corrosion behavior of Fe-based shape memory alloys *Corros. Sci.* **44** 2013–26
- [26] Joo J, Kang M, Shin D, Seo E, Kim D, Yeon Y, Hong K, Lee W and Lee J 2020 Corrosion resistance of shape recoverable Fe-17Mn-5Si-5Cr Alloy in concrete structures *Materials (Basel)*. **13** 5531
- [27] Farhat H, Griffin R, Oguocha I N A and Evitts R 2018 An investigation of the corrosion behaviour of a FeNiCoAlTa shape memory alloy in 3.5 wt-% NaCl solution *Corros. Eng. Sci. Technol.* **53** 611–6
- [28] Zhang X, Cui T, Liu Q, Dong Z and Man C 2021 Effect of Nd addition on the microstructure,

- mechanical properties, shape memory effect and corrosion behaviour of Cu–Al–Ni high-temperature shape memory alloys *J. Alloys Compd.* **858** 157685
- [29] Dawood N M and Abid Ali A R 2021 Influence of Titanium Additions on the Corrosion Behavior of Cu-Al-Ni Shape Memory Alloys *Materials Science Forum* vol 1021 (Trans Tech Publ) pp 55–67
- [30] Mishra R K, Sahay P P and Shahi R R 2019 Alloying, magnetic and corrosion behavior of AlCrFeMnNiTi high entropy alloy *J. Mater. Sci.* **54** 4433–43
- [31] Zhang Y, Jiang X, Sun H and Shao Z 2020 Effect of annealing heat treatment on microstructure and mechanical properties of nonequiatomic CoCrFeNiMo medium-entropy alloys prepared by hot isostatic pressing *Nanotechnol. Rev.* **9** 580–95
- [32] Nawaz T, Ali A, Ahmad S, Piatkowski P and Alnaser A S 2023 Enhancing Anticorrosion Resistance of Aluminum Alloys Using Femtosecond Laser-Based Surface Structuring and Coating *Nanomaterials* **13**
- [33] Ali A, Piatkowski P, Nawaz T, Ahmad S, Ibrahim T, Khamis M and Alnaser A S 2023 A Two-Step Femtosecond Laser-Based Deposition of Robust Corrosion-Resistant Molybdenum Oxide Coating *Materials (Basel)*. **16**
- [34] Mohamed O, Hassan M, Egilmez M, Abuzaid W, Ibrahim T and Khamis M 2022 Corrosion behavior of CoCrNi/mild steel medium entropy alloy thin films *Mater. Today Commun.* **30** 103015
- [35] Ahmad S, Ahmad W, Abu Baker A, Egilmez M, Abuzaid W, Orhan M F, Ibrahim T, Khamis M and Alnaser A S 2022 Enhancement of the corrosion resistance of mild steel with femtosecond laser- nanostructuring and CrCoNi medium entropy alloy coating *Appl. Surf. Sci. Adv.* **12** 100321